Electrochemical Performance of Lanthanum Cerium Ferrite Nanoparticles for Supercapacitor Applications

Waseem Raza (waseemrazaphysics@gmail.com)
University of Gujrat - Hafiz Hayat Campus: University of Gujrat https://orcid.org/0000-0002-6307-6614
Ghulam Nabi
University of Gujrat Faculty of Sciences
Asim Shahzad
Quaid-e-Azam University, Islamabad
Nafisa Malik
University of Gujrat
Nadeem Raza
University of Gujrat

Original Research

Keywords: Hydrothermal, Co-precipitation synthesis, LaCeFe2O4, Specific Capacitance, Supercapacitors

Posted Date: February 4th, 2021

DOI: https://doi.org/10.21203/rs.3.rs-160990/v1

Version of Record: A version of this preprint was published at Journal of Materials Science: Materials in Electronics on February 20th, 2021. See the published version at https://doi.org/10.1007/s10854-021-05457-w.

Abstract

Lanthanum cerium ferrite nanoparticles has been synthesized for the first time via hydrothermal and co-precipitation method. The structural and morphological study of the nanoparticles have been examined by using X-ray powder diffraction (XRD), scanning electron microscopy (SEM), transmission electron microscopy (TEM) and energy dispersive x-ray spectroscopy (EDX). The electrochemical study of J1 and J2 electrodes have been examined using three electrode system in 6 M KOH electrolyte using cyclic voltammetry (CV), galvanostatic charging-discharging (GCD) and electrochemical impendence spectroscopy (EIS). The highest specific capacitance of 1195 F/g has been obtained at a scan rate of 10 mV/s from hydrothermal synthesis nanomaterial electrode (J2) and long cycling life 92.3% retention after 2000^{th} cycles. Furthermore, the energy density and power density of the J2 electrode at a current density of 5 A/g was 59 Wh/kg and 9234 W/kg respectively. Hence, the fabricated J2 electrode is a favorable candidate for super-capacitor applications.

1. Introduction

Supercapacitors are highly convenient in such applications where high power density and short charging time is required such as in power emergency actuators in airlines, in hybrid electric vehicles, photographic flashes, electric screwdriver, gondolas and high power devices [1]. Supercapacitors also have played a significant role to stabilize the power supply and voltage in numerous industries where load fluctuation is the major issue [2]. Moreover, flexible supercapacitors are used in both wearable and portable electronic through twisting and folding conditions [3]. A supercapacitor consists of two electrodes, a separator and an electrolyte. It is divided in to two main categories owing to charge storage mechanism; electric double layer capacitors (EDLCs) and pseudocapacitors. EDLCs are stored charge at the electrode/electrolyte interface by physical adsorption/desorption and it depends on the contact surface between electrode and electrolyte. In the start, EDLCs electrodes were made using conducting polymers, metal oxides and lithium ions materials whereas currently researcher are widely using, carbon nanotubes (CNTs), graphene and activated carbon because these materials have many remarkable properties such as lightweight, large surface areas, excellent conductivity and electrochemical stability [4, 5]. Faradic reactions (oxidation–reduction reactions) are used in pseudocapacitors to store charge nearby the surface and inside the bulk of the electrodes [6]. Pseudocapacitors electrodes are made by using conducting polymers, transition metal oxides and transition metal oxides composites. The major drawback of pseudocapacitors is shorter lifetime as compare to EDLCs [7, 8]. T. Brousse et al, reported that metal oxide has been studied for use in pseudo-capacitors such as RuO, PbO_2, $Ni(OH)_2$, MnO_2 [9] because these materials contain various corrosion state which make possible the faradic arraign relocate mechanism. In the literature, the authors reported that only the precious metal oxide has shown good stability such as RuO and IrO. But both of these are very expensive metals [10]. By contrast, MnO_2 has been reported high theoretical capacitances in the range of 1100 to 1300 Fg^{-1}, less toxic and much low in cost [11, 12]. Poor cycling stability of MnO_2 is the major problem for using it as a pseudo-capacitor material [13]. The electrolytes used in supercapacitors are mainly divided into three categories solid-state electrolytes, liquid-state

electrolytes and gel-state electrolytes. Solid based electrolytes supercapacitors are prevented from leaking, but their interaction between electrolyte and electrode is poor. However, in liquid-state electrolytes the major problem is leakage so that's why commonly the gel-state electrolytes are used during the fabrication of supercapacitors [14, 15].

In the literature many authors reported that ferrites are chemically and thermally stable in the range of nanometer scale and displays unexpected behavior both in chemical and physical properties [16]. In many applications cobalt ferrites are most suitable such as gas sensors [17], pigments [18], photocatalysts [19], magnetic resonance imaging [20], and in electrochemical energy storage devices [21, 22]. Furthermore, the ferrites properties can be improved by doping/substitution of other metallic elements (i.e., iron, cobalt, cerium, aluminum) in octahedral and tetrahedral sites.

Doping is a noteworthy and more effective technique to well tune the desired properties of semiconductors. The dopant can be improved electrochemical properties of ferrites semiconductors nanomaterial by shifting energy band structure, tuning the morphology, producing additional active sites at the grain boundaries and enhance the surface to volume ratio [23].

For both Li-ion battery and super-capacitor applications spinel ferrites MFe_2O_4 (M = Co, Ni, Zn, Fe, Cu, etc.) as well as their nano-composites have been used as a potential material [24-26]. They are abundant in nature, inexpensive, environment-friendly and stable. A number of researchers have been reported that electrochemical performance of spinel ferrites nanomaterials can be improved with doping of various elements [27-29] such as $MxFe_{3-x}O_4$ (M = Fe, Cu, Co, Mn), $Mn_xCo_{3-x}O_4$, [30] $LaNi_{1-x}Mg_xO_3$, [31] and $CuxCo_{3-x}O_4$ [32] for super-capacitor electrode.

Magnetic spinel ferrites have been fascinated the researchers owing to their extended applications in many fields for instance water splitting, magnetic recording, biomedical and magnetic recording [33-36]. Ferrites nanomaterials are synthesized using plenty of methods such as sol-gel, co-precipitation, hydrothermal route, ball milling, electrospinning, polyol route, micro-emulsion, dip coating and molten-salt method. Among the several methods, hydrothermal method is low-cost, less toxic, and eco-friendly as compare to other techniques [37-45].

In this article a new lanthanum cerium ferrite ($LaCeFe_2O_4$) has been synthesized highly porous nanoparticles through two different synthesis methods involving "chemical co-precipitation and hydrothermal methods" as an electrode material for supercapacitor. The surface morphology, structure and elemental composition of the synthesized materials by scanning electron microscopy (SEM), X-ray diffraction (XRD), and energy dispersive x-ray spectroscopy (EDX) have been studied. Furthermore, the electrochemical capacitive behavior of lanthanum cerium ferrite ($LaCeFe_2O_4$) electrodes have been investigated via cyclic voltammetry (CV), galvanostatic charging/discharging (GCD) and electrochemical impendence spectroscopy (EIS) in 6 M KOH electrolyte. The synthesize materials have exhibited a noteworthy specific capacitance (C_{sp}) and cycling stability as compare to previously reported ferrites materials.

2. Experimental Part

2.1 Materials

Cerium nitrate hexahydrate {$Ce(NO_3)_3.6H_2O$}, lanthanum nitrate hexahydrate {$La(NO_3)_3.6H_2O$}, ferric nitrate nonahydrate {$Fe(NO_3)_3.9H_2O$}, sodium hydroxide (NaOH) and absolute ethanol (C_2H_5OH) were obtained from sigma-aldrich. In this study, without any further sanitization all the chemicals have used.

2.2 Co-precipitation method for $LaCeFe_2O_4$

Initially, three solutions were prepared through adding 0.3 mole of $Fe(NO_3)_3.9H_2O$, 0.05 mole of $La(NO_3)_3.6H_2O$ and 0.05 mole of $Ce(NO_3)_3.6H_2O$ in 20 ml distilled water respectively. Then, all the solutions were mixed together under constant stirring at room temperature for 15 minutes to get homogeneous mixture and named A. In the next step, 02 mole of NaOH was dissolved in 25 ml distilled water used as a precipitating agent and added drop wise into solution A with the help of burette under constant stirring at 80^oC for 3 hours. Brick red precipitates were formed, when whole the NaOH solution was added into solution A. At the end, the formed precipitates were washed six times with ethanol and distilled water and dried in an oven at 200^oC for 24 hours. In this process, the synthesize material was named as J1. The schematic diagram of co-precipitate method was shown in fig. 1.

2.3 Hydrothermal method for $LaCeFe_2O_4$

First, three solutions were prepared through adding 0.3 mole of $Fe(NO_3)_3.9H_2O$, 0.05 mole of $La(NO_3)_3.6H_2O$ and 0.05 mole of $Ce(NO_3)_3.6H_2O$ in 20 ml distilled water respectively. Then, all the solutions were mixed together under constant stirring at room temperature for 30 minutes to get homogeneous mixture and named A. After that, 02 mole of NaOH was dissolved in 25 ml distilled water as a precipitating agent and added drop wise into solution A with the help of burette. When whole the NaOH solution was added into solution A, its color was changed into brick red and named B. In the next step, solution B was shifted to Teflon lined (TL) autoclave and kept in an oven and heating at 140^oC for 18 hours. At the end, the obtained final product was cool down and six times with ethanol and distilled water and dried in an oven at 200^oC for 24 hours. In this process, the synthesize material was named as J2. The schematic diagram of hydrothermal method was shown in fig. 2.

2.5 Morphological and structural characterization

The morphology of the synthesized nanomaterial have been examined using scanning electron microscopy (SEM, LEO 1450 VP) and transmission electron microscopy (TEM, JEOL JEM-2100) operating at an accelerating voltage of 2000 V respectively.

The elemental composition has been examined using an energy dispersive x-ray spectroscopy (EDX, EAG AN461). The crystal structure of $LaCeFe_2O_4$ nanostructures have been examined by means of X-ray powder diffraction (XRD, Rigaku, CuKα, λ = 1.5418 A˚).

2.6 Electrode fabrication and electrochemical measurements

All the working electrodes (WE) were fabricated using $LaCeFe_2O_4$ as an active material which was synthesized via co-precipitate and hydrothermal method. A homogeneous slurry was formed by mixing 80% active material {$LaCeFe_2O_4$ (80 wt%, 30.5mg)}, 15% (15 wt%, 5.5mg) carbon black as conducting material and 5% (15 wt%, 5.5mg) polyvinylidene fluoride (PVDF) as binding agent under constant stirring at room temperature for 12 hours. After that, a homogeneous slurry of 80mg was coated on the nickel foam (current collector) area 1-cm^2. Finally, the fabricated electrode was dried in an oven at 100^oC for 20 hours. The fabricated $LaCeFe_2O_4$ working electrodes were analyzed by three electrode system involving a working electrode ($LaCeFe_2O_4$), a counter electrode (platinum wire) and a reference electrode (Ag-AgCl) respectively. Gamry e5000 potentiostat was used to analyze all the electrochemical measurements such as cyclic Voltammetry (CV), galvanostatic charging/discharging (GCD) and electrochemical impendence spectroscopy (EIS) in a 6 M KOH electrolyte under environmental conditions. The CV measurements were recorded in the potential window 0.1-0.6 V at different scan rates. The GCD tests were recorded at different current densities 5 A/g to 25 A/g in a constant potential window 0.1-0.6 V. The EIS tests were performed within open circuit potential in the frequency range of 100 kHz to 10 mHz. The specific capacitance C_{sp} (F/g) from CV and GCD were calculated by using the equation (1) [27, 46] and (2) [47, 48] respectively.

$$C_{sp} = \frac{\int IdV}{mv\Delta V} \quad (1)$$

$$C_{sp} = \frac{I\Delta t}{m\Delta V} \quad (2)$$

Where I is the current (A), m is the mass of active material (mg), is the potential window (ΔV), v is the scan rate (mV/s) and Δt is the discharge time (s).

The power density E_d (Wh/kg) and energy density P_d (W/kg) of the $LaCeFe_2O_4$ supercapacitor were calculated by using equation (3) and (4) [48, 49] respectively.

$$E_d = \frac{1}{2} C_{sp} \Delta V^2 \quad (3)$$

$$P_d = \frac{Ed}{\Delta V} \quad (4)$$

Where I is the current (A), m is the mass of active material (kg), ΔV is the potential window (V), and Δt is the discharge time (h).

3. Results And Discussion

The morphology of $LaCeFe_2O_4$ nanostructures have been examined by using scanning electron microscopy (SEM) and transmission electron microscopy (TEM). Both co-precipitation and hydrothermal method synthesized $LaCeFe_2O_4$ nanostructures micrographs are shown in fig. 3(a-b). The micrograph of co-precipitate method shows that nanoparticles are formed on the other hand the micrograph of hydrothermal method displays that agglomeration formation of porous nanoparticles is formed. The agglomeration in the nanoparticles is formed may be due to interfacial surface tension [50]. TEM image of the hydrothermal method synthesized $LaCeFe_2O_4$ nanoparticles are shown in fig .3(c). It shows that the uniformly distributed spherical nanoparticles having a diameter in the range of 160-180 nm. This nanoparticles like morphology of $LaCeFe_2O_4$ with high surface area might produce additional active sites for more efficient contact between the surface of electrode material and electrolyte ions which can improve the electrochemical process and capacitive ability of the nanostructures. The chemical composition of both J1 and J2 samples have been examined by using energy dispersive X-rays spectroscopy (EDX) and spectrum is shown in Fig. 3(d-e). The weight and atomic percentage of the elements present in JI and J2 nanostructures has shown in the table (inset of Fig. 3(d-e). These ratios confirm that the lanthanum and cerium are close to stoichiometry, which is in good agreement with the 1:1 ratios of lanthanum and cerium in ferrites. More interestingly, the EDX spectrum has represented that no impurity element present in both J1&J2 nanostructure sample.

X-rays diffraction patterns of synthesized lanthanum cerium ferrite ($LaCeFe_2O_4$) through co-precipitate and hydrothermal method are shown in fig. 4. The XRD patterns containing four prominent scattering peaks in the 2 theta range of 20°–80° which corresponds to the crystal planes (111), (200), (220) and (311) demonstrating the formation of cubic lanthanum cerium ferrite structure (space group Fd3m). The XRD patterns are good agreement with JCPDS card (22-1086) and (81-0792) [51, 52]. Furthermore, the XRD patterns (fig. 5) represent the considerable contraction of the peaks of J2 sample, which is indication of the formation of large crystallites. More interestingly, it can be seen that no extra peaks are observed in both the samples of XRD patterns (J1 and J2) which represents the formation of pure $LaCeFe_2O_4$ nanoparticles without calcination. Moreover, the J2 (hydrothermal process preparation) sample peaks have highly sharpness and more intensity as compere to J1 (co-precipitation process preparation) sample which are indicating the well crystalline nature of the J2 sample therefore hydrothermal route synthesized $LaCeFe_2O_4$ nanoparticles are more suitable for supercapacitor electrode material.

The as-fabricated $LaCeFe_2O_4$ nanoparticles electrochemical capacitive performance has been investigated via CV and GCD tests. The CV curves of J1 and J2 nanoparticles have been tested at a scan rate of 15mV/s in the potential range of 0.1 to 0.6 V by using 6 M KOH electrolyte are shown in Fig. 5(a).

The CV curves of both the samples J1 and J2 indicate the Faradic type capacitive features, for J1 sample two peaks are observed at ~ 0.44 V and ~0.33 V for the oxidation and the reduction processes respectively, while for J2 sample three peaks are observed in which one peak for oxidation process (~0.52 V) and two peaks for reduction process (~0.32 V and ~0.38 V) respectively. There might be two main reasons for the observation of three peaks in J2 sample (1) both lanthanum and cerium have various oxidation states and (2) formation of highly pores and more active sites nanoparticles via hydrothermal method. The specific capacitance (C_{sp}) of J1 and J2 sample at a scan rate of 15mV/s were obtained from equation (1) are shown in Fig. 6(a). In addition, to get more information about the electrochemical behavior of J2 sample, CV tests were recorded at different scan rates in the potential range of 0.1 to 0.6 V in 6 M KOH electrolyte are shown in Fig. 5(b). It could be observed that with the increase of scan rate the area under the curves gradually increases. This represents that scan rates are directly proportional to the CV current, which exhibit the ideal behavior of capacitive [53]. Moreover, the specific capacitance calculated from CV curves from the equation (1) is also dependent on the scan rate. The maximum specific capacitance C_{sp} (1195 F/g) was obtained at the lowest scan rate (10mV/s), while minimum specific capacitance C_{sp} (1020 F/g) was obtained at the highest scan rate (50mV/s). This could be attributed that more ohmic resistance occur at larger scan rates [54]. Furthermore, Fig. 5(b) represents the couples of different boarding redox peaks analogous to the redox rare earth elements of La_{3+}/ La_{2+} and Ce_{3+}/ Ce_{2+}. The redox processes related to the Faradic capacitive behavior of $LaCeFe_2O_4$ nanoparticles could proceed according to equations (7) [55] and (8) [49].

La_{3+}/ La_{2+} system: $LaFe_2O_4 + OH + H_2O \rightarrow 2FeOOH + LaOOH + e$ (7)

Ce_{3+}/ Ce_{2+} system: $CeFe_2O_4 + OH + H_2O \rightarrow 2FeOOH + CeOOH + e$ (8)

The CV curves (Fig. 5(a-b)) show the same behavior at different scan rates, which illuminating the reversibility of the redox reactions. The comparative specific capacitance C_{sp} (F/g) of J1 and J2 electrodes at scan rate of 15mV/s in the potential range of 0.1-0.6 V in 6 M KOH electrolyte are shown in Fig. 6(a) and the obtained specific capacitance C_{sp} from other different scan rates are shown in Fig. 6(b).

All the GCD curves of J2 ($LaCeFe_2O_4$) electrode show the deviations from linearity owing to the pseudo-capacitive nature which is good agreement with CV results. Fig. 7 represent the energy losses arising due to equivalent series resistance or internal resistance in the charging and discharging curves are indicated the IR drop at the turning point [56]. Furthermore, the specific capacitance is progressively decrease with increasing discharge current density due to increasing of IR drop.

The specific capacitance C_{sp} (F/g) from GCD curves were calculated at different current densities by using equation (2) and are shown in Fig. 8 (a). Power density (P_d) and energy density (E_d) are two important parameters to investigate the electrochemical performance of supercapacitor electrode materials. The power density P_d (W/kg) and energy density E_d (Wh/kg) from GCD curves were calculated

at different current densities via equation (3) and (4) respectively. Ragone plot obtained from GCD curves at different current densities for J2 electrode are shown in Fig. 8(b). More interestingly, the supercapacitor performance parameters such as specific capacitance (C_{sp}) Power density (P_d) and energy density (E_d) with some other reported ferrite based materials are given in Table 1. It could be noted that J2 electrode is superior to previous reported ferrites.

Table 1. Supercapacity performance of $LaCeFe_2O_4$ Compare With Some Other Ferrite Based Materials.

Material	Synthesis Method	Electrolyte	Cs (F/g)	E (Wh/kg)	P (W/kg)	Reference
$NiCoFe_2O_4$	Sol-gel	1 M KOH	50	4.79	1426.23	[57]
$NiCuFe_2O_4$	Sol-gel	1 M KOH	44	4.62	1000.99	[57]
$CuCoFe_2O_4$	Sol-gel	1 M KOH	76.90	7.90	1711.95	[57]
$CuCoFe_2O_4$	Sol-gel	1 M KOH	397	3.53	198.50	[52]
$Al_xCu_yCo_zFe_2O_4$ (x + y+ z = 1)	Sol-gel	1 M KOH	256-540	0.58-8.42	128-270	[52]
$MnCoFe_2O_4$	Co-precipitation	6 M KOH	675	3.15	2250.00	[58]
$LaCeFe_2O_4$	Co-precipitation	6 M KOH	780	-	-	**This work**
$LaCeFe_2O_4$	Hydrothermal	6 M KOH	1180	59.00	9234.00	**This work**

Cyclic stability is another significant parameter because it is used to determine the durability and efficiency of supercapacitor [59]. The cycling measurements for J2 electrode has been studied via CV tests for 2000 cycles at the scan rate of 10 mV/s and are shown in Fig 9. The J2 electrode shows 92.3% capacitance retention after 2000^{th} cycles, which indicates the high rate of capability and electrochemical long term cycling stability.

Electrochemical impedance spectroscopy (EIS) measurement of J1 and J2 electrodes have been tested within open circuit potential in the frequency range of 100 kHz to 10 mHz in 6 M KOH electrolyte and Nyquist plot are shown in Fig. 10. Inset of Fig. 10 shows the fitted Nyquist plot equivalent circuit which consists of Warburg impedance (Wo), solution resistance (R_s) charge transfer resistance (R_{ct}) and constant phase element (CPE) to examine the capacitive behavior.

High frequency intercept on the real axis shows the solution resistance (Rs) which contains an intrinsic resistance of substrate, contact resistance of active material and ionic resistance of electrolyte however semicircular arc represents the charge transfer resistance (R_{ct}) between electrode and electrolyte interface

and a constant phase element (CPE) shows the non-ideal double layer capacitance. The Warburg impedance (Wo) indicating the frequency dependence diffusion resistance of ions electrolyte. The fitted values of EIS spectra for both J1 and J2 electrodes are given in Table 2. Which indicating the J2 electrode have a worthy response as compare to J1 electrode. Hence, J2 electrode is a promising contender for supercapacitors.

Table 2. The fitted values of EIS spectra for both J1 and J2 electrodes

Parameters	J1 electrode	J2 electrode
Solution resistance (Rs)	1.69 Ω	1.74 Ω
Charge transfer resistance (Rct)	31.72 Ω	55.42 Ω
Warburg impedance (W0)	72.19 $\Omega s^{-0.5}$	68.32 $\Omega s^{-0.5}$

Conclusions

$LaCeFe_2O_4$ nanoparticles were synthesized using two simple methods “co-precipitate and hydrothermal process” and examined as a potential material for supercapacitor electrodes. The structural and electrochemical properties of the $LaCeFe_2O_4$ nanoparticles were studied. XRD patterns were conformed to the formation of single-phase ferrite. SEM micrographs was conformed to the formation of porous nanoparticles that enable charge transfer of electrolyte. TEM study was conformed to the uniformly distributed spherical nanoparticles having diameter in the range of 160-180 nm. EDX spectrums were shown the formation of $LaCeFe_2O_4$ without any impurity element. The fabricated electrodes of $LaCeFe_2O_4$ electrodes were investigated in 6 M KOH electrolyte via CV,GCD and EIS. The electrochemical properties of hydrothermal method synthesis $LaCeFe_2O_4$ nanoparticles was shown a good Faradaic behavior, with a high specific capacitance of 1195 F/g at a scan rate of 10 mV/s. The cyclic stability was studied via CV and the capacitance retention was 92.3% after 2000 cycles. The energy and power density of the $LaCeFe_2O_4$ supercapacitor electrode at a current density of 5 A/g was 59 Wh/kg and 9234 W/kg respectively. The EIS study also confirmed that J2 electrode have a good response as compare to J1 electrode.

Declarations

Waseem Raza: Conceptualization, Methodology, Investigation and performed the whole experiments also wrote the manuscript. **Ghulam Nabi:** Supervision, Resources. **Asim Shahzad:** Writing - review & editing, Data curation. **Nafisa Malik:** Writing - review & editing. **Nadeem Raza:** Discussed the characterizations and reviewed the manuscript. The authors read and approved the final manuscript.

Declarations

All authors declare that there is no conflict of interest.

Acknowledgement

The author (Dr. Ghulam Nabi) acknowledge the Higher Education Commission (HEC) of Pakistan, for providing funding under NRPU Research Project No.6502 and 6510.

References

1. Zou, T., et al., *Improvement of the electrochemical performance of Li1. 2Ni0. 13Co0. 13Mn0. 54O2 cathode material by Al2O3 surface coating.* Journal of Electroanalytical Chemistry, 2020: p. 113845.
2. Khan, J. and U. Nasir, *Voltage stabilization of hybrid micro-grid using super capacitors.* Journal of Power and Energy Engineering, 2015. **3**(06): p. 1.
3. Nabi, G., et al., *Cogent synergic effect of TiS2/g-C3N4 composite with enhanced electrochemical performance for supercapacitor.* Ceramics International, 2020. **46**(17): p. 27601-27607.
4. Afzal, A., et al., *Polypyrrole/carbon nanotube supercapacitors: Technological advances and challenges.* Journal of Power Sources, 2017. **352**: p. 174-186.
5. Lobato, B., et al., *Capacitance and surface of carbons in supercapacitors.* Carbon, 2017. **122**: p. 434-445.
6. Soin, N., et al., *Nanocrystalline ruthenium oxide dispersed Few Layered Graphene (FLG) nanoflakes as supercapacitor electrodes.* Journal of Materials Chemistry, 2012. **22**(30): p. 14944-14950.
7. Wang, Y., Y. Song, and Y. Xia, *Electrochemical capacitors: mechanism, materials, systems, characterization and applications.* Chemical Society Reviews, 2016. **45**(21): p. 5925-5950.
8. Wang, S., et al., *Facile preparation of Ni–Mn layered double hydroxide nanosheets/carbon for supercapacitor.* Journal of Materials Science: Materials in Electronics, 2019. **30**(8): p. 7524-7533.
9. Hosseini, H. and S. Shahrokhian, *Vanadium dioxide-anchored porous carbon nanofibers as a Na+ intercalation pseudocapacitance material for development of flexible and super light electrochemical energy storage systems.* Applied Materials Today, 2018. **10**: p. 72-85.
10. Brousse, T., D. Bélanger, and J.W. Long, *To be or not to be pseudocapacitive?* Journal of The Electrochemical Society, 2015. **162**(5): p. A5185-A5189.
11. Devaraj, S. and N. Munichandraiah, *High capacitance of electrodeposited MnO2 by the effect of a surface-active agent.* Electrochemical and Solid-State Letters, 2005. **8**(7): p. A373-A377.
12. Toupin, M., T. Brousse, and D. Bélanger, *Influence of microstucture on the charge storage properties of chemically synthesized manganese dioxide*. Chemistry of Materials, 2002. **14**(9): p. 3946-3952.
13. Qi, J., et al., *Facile synthesis of N-doped activated carbon derived from cotton and CuCo 2 O 4 nanoneedle arrays electrodes for all-solid-state asymmetric supercapacitor.* Journal of Materials Science: Materials in Electronics, 2019. **30**(10): p. 9877-9887.
14. Shieh, J.-Y., et al., *High-performance flexible supercapacitor based on porous array electrodes.* Materials Chemistry and Physics, 2017. **195**: p. 114-122.

15. Obeidat, A.M., M.A. Gharaibeh, and M. Obaidat, *Solid-state supercapacitors with ionic liquid gel polymer electrolyte and polypyrrole electrodes for electrical energy storage.* Journal of Energy Storage, 2017. **13**: p. 123-128.
16. Gonsalves, L., S. Mojumdar, and V. Verenkar, *Synthesis and characterization of Co0. 8Zn0. 2Fe2O4 nanoparticles.* Journal of thermal analysis and calorimetry, 2011. **104**(3): p. 869-873.
17. Rao, P., R. Godbole, and S. Bhagwat, *Copper doped nickel ferrite nano-crystalline thin films: a potential gas sensor towards reducing gases.* Materials Chemistry and Physics, 2016. **171**: p. 260-266.
18. Sebastian, R., et al., *Structural and dielectric studies of Cr3+ doped ZnFe2O4 nanoparticles.* Nano Stud, 2013. **8**: p. 121-130.
19. Hwang, C.-S. and N.-C. Wang, *Preparation and characteristics of ferrite catalysts for reduction of CO2.* Materials chemistry and physics, 2004. **88**(2-3): p. 258-263.
20. Manikandan, A., et al., *Optical and magnetic properties of Mg-doped ZnFe2O4 nanoparticles prepared by rapid microwave combustion method.* Superlattices and Microstructures, 2013. **64**: p. 118-131.
21. Khandekar, M., et al., *Nanocrystalline Ce doped CoFe2O4 as an acetone gas sensor.* Ceramics International, 2014. **40**(1): p. 447-452.
22. Lin, Y., et al., *Deposition of polyaniline on porous ZnFe 2 O 4 as electrode for enhanced performance supercapacitor.* Journal of Materials Science: Materials in Electronics, 2018. **29**(19): p. 16369-16377.
23. Bodade, A.B., et al., *Conduction mechanism and gas sensing properties of CoFe2O4 nanocomposite thick films for H2S gas.* Talanta, 2012. **89**: p. 183-188.
24. Kumbhar, V., et al., *Chemical synthesis of spinel cobalt ferrite (CoFe2O4) nano-flakes for supercapacitor application.* Applied Surface Science, 2012. **259**: p. 39-43.
25. He, P., et al., *Reduced graphene oxide-CoFe 2 O 4 composites for supercapacitor electrode.* Russian Journal of Electrochemistry, 2013. **49**(4): p. 359-364.
26. Zhang, Y.X., et al., *One-pot controllable synthesis of flower-like CoFe2O4/FeOOH nanocomposites for high-performance supercapacitors.* Materials Letters, 2014. **123**: p. 229-234.
27. Xiong, P., H. Huang, and X. Wang, *Design and synthesis of ternary cobalt ferrite/graphene/polyaniline hierarchical nanocomposites for high-performance supercapacitors.* Journal of power sources, 2014. **245**: p. 937-946.
28. Huang, J., et al., *Effect of Al-doped β-Ni (OH) 2 nanosheets on electrochemical behaviors for high performance supercapacitor application.* Journal of Power Sources, 2013. **232**: p. 370-375.
29. Ghassemi, N., S.S.H. Davarani, and H.R. Moazami, *Cathodic electrosynthesis of CuFe 2 O 4/CuO composite nanostructures for high performance supercapacitor applications.* Journal of Materials Science: Materials in Electronics, 2018. **29**(15): p. 12573-12583.
30. Rios, E., et al., *Mixed valency spinel oxides of transition metals and electrocatalysis: case of the MnxCo3− xO4 system.* Electrochimica Acta, 1998. **44**(8-9): p. 1491-1497.

31. Du, Z., et al., *Electrocatalytic performances of LaNi1− xMgxO3 perovskite oxides as bi-functional catalysts for lithium air batteries.* Journal of Power Sources, 2014. **265**: p. 91-96.
32. De Koninck, M., S.-C. Poirier, and B. Marsan, *Cu x Co3− x O4 Used as Bifunctional Electrocatalyst Physicochemical properties and electrochemical characterization for the oxygen evolution reaction.* Journal of The Electrochemical Society, 2006. **153**(11): p. A2103-A2110.
33. Abu-Dief, A.M., et al., *Effect of chromium substitution on the structural and magnetic properties of nanocrystalline zinc ferrite.* Materials Chemistry and Physics, 2016. **174**: p. 164-171.
34. Afghahi, S.S.S., et al., *Single and double-layer composite microwave absorbers with hexaferrite BaZn0. 6Zr0. 3X0. 3Fe10. 8O19 (X= Ti, Ce, Sn) powders.* Materials Chemistry and Physics, 2017. **186**: p. 584-591.
35. Shaheen, W., *Effects of thermal treatment and doping with cobalt and manganese oxides on surface and catalytic properties of ferric oxide.* Materials chemistry and physics, 2007. **101**(1): p. 182-190.
36. Gupta, A.K. and M. Gupta, *Synthesis and surface engineering of iron oxide nanoparticles for biomedical applications.* biomaterials, 2005. **26**(18): p. 3995-4021.
37. Nogueira, N., et al., *X-ray diffraction and Mossbauer studies on superparamagnetic nickel ferrite (NiFe2O4) obtained by the proteic sol–gel method.* Materials Chemistry and Physics, 2015. **163**: p. 402-406.
38. Islam, M., et al., *Electrical transport properties of CoZn ferrite–SiO2 composites prepared by co-precipitation technique.* Materials Chemistry and Physics, 2008. **109**(2-3): p. 482-487.
39. Yang, Z., Z. Li, and Y. Yang, *Structural and magnetic properties of plate-like W-type barium ferrites synthesized with a combination method of molten salt and sol–gel.* Materials Chemistry and Physics, 2014. **144**(3): p. 568-574.
40. Kurtan, U., et al., *Synthesis and magneto-electrical properties of MFe2O4 (Co, Zn) nanoparticles by oleylamine route.* Ceramics International, 2016. **42**(12): p. 13350-13358.
41. Töpfer, J. and A. Angermann, *Nanocrystalline magnetite and Mn–Zn ferrite particles via the polyol process: Synthesis and magnetic properties.* Materials Chemistry and Physics, 2011. **129**(1-2): p. 337-342.
42. Bid, S. and S. Pradhan, *Preparation of zinc ferrite by high-energy ball-milling and microstructure characterization by Rietveld's analysis.* Materials Chemistry and Physics, 2003. **82**(1): p. 27-37.
43. Rehman, J., et al., *Structural, magnetic and dielectric properties of terbium doped NiCoX strontium hexagonal nano-ferrites synthesized via micro-emulsion route.* Ceramics International, 2016. **42**(7): p. 9079-9085.
44. Azhagushanmugam, S., N. Suriyanarayanan, and R. Jayaprakash, *Magnetic properties of zinc-substituted cobalt ferric oxide nanoparticles: correlation with annealing temperature and particle size.* Materials science in semiconductor processing, 2014. **21**: p. 33-37.
45. Schütz, A., et al., *High temperature (salt melt) corrosion tests with ceramic-coated steel.* Materials Chemistry and Physics, 2015. **159**: p. 10-18.

46. Bindu, K., et al., *Microwave assisted growth of stannous ferrite microcubes as electrodes for potentiometric nonenzymatic H2O2 sensor and supercapacitor applications.* Electrochimica Acta, 2016. **217**: p. 139-149.
47. Vadiyar, M.M., et al., *Reflux condensation mediated deposition of Co3O4 nanosheets and ZnFe2O4 nanoflakes electrodes for flexible asymmetric supercapacitor.* Electrochimica Acta, 2016. **222**: p. 1604-1615.
48. Liu, L., et al., *Binary cobalt ferrite nanomesh arrays as the advanced binder-free electrode for applications in oxygen evolution reaction and supercapacitors.* Journal of Power Sources, 2016. **327**: p. 599-609.
49. Xiong, P., et al., *Ternary manganese ferrite/graphene/polyaniline nanostructure with enhanced electrochemical capacitance performance.* Journal of Power Sources, 2014. **266**: p. 384-392.
50. Sundararajan, M., et al., *Microwave combustion synthesis of zinc substituted nanocrystalline spinel cobalt ferrite: structural and magnetic studies.* Materials Science in Semiconductor Processing, 2015. **40**: p. 1-10.
51. Nabi, G., et al., *Role of cerium-doping in CoFe2O4 electrodes for high performance supercapacitors.* Journal of Energy Storage, 2020. **29**: p. 101452.
52. Bhujun, B., M.T. Tan, and A.S. Shanmugam, *Evaluation of aluminium doped spinel ferrite electrodes for supercapacitors.* Ceramics International, 2016. **42**(5): p. 6457-6466.
53. Gujar, T., et al., *Electrochemically deposited nanograin ruthenium oxide as a pseudocapacitive electrode.* Int. J. Electrochem. Sci, 2007. **2**: p. 666-673.
54. Pawar, D., et al., *Synthesis of nanocrystalline nickel–zinc ferrite (Ni0. 8Zn0. 2Fe2O4) thin films by chemical bath deposition method.* Journal of Alloys and Compounds, 2011. **509**(8): p. 3587-3591.
55. Hao, J., et al., *Facile synthesis of 3D hierarchical flower-like Co3-xFexO4 ferrite on nickel foam as high-performance electrodes for supercapacitors.* Electrochimica Acta, 2015. **152**: p. 13-18.
56. Fan, Z., et al., *Asymmetric supercapacitors based on graphene/MnO2 and activated carbon nanofiber electrodes with high power and energy density.* Advanced Functional Materials, 2011. **21**(12): p. 2366-2375.
57. Bhujun, B., M.T. Tan, and A.S. Shanmugam, *Study of mixed ternary transition metal ferrites as potential electrodes for supercapacitor applications.* Results in Physics, 2017. **7**: p. 345-353.
58. Elkholy, A.E., F.E.-T. Heakal, and N.K. Allam, *Nanostructured spinel manganese cobalt ferrite for high-performance supercapacitors.* RSC advances, 2017. **7**(82): p. 51888-51895.
59. Guo, P., et al., *Electrochemical properties of colloidal nanocrystal assemblies of manganese ferrite as the electrode materials for supercapacitors.* Journal of Materials Science, 2017. **52**(9): p. 5359-5365.

Figures

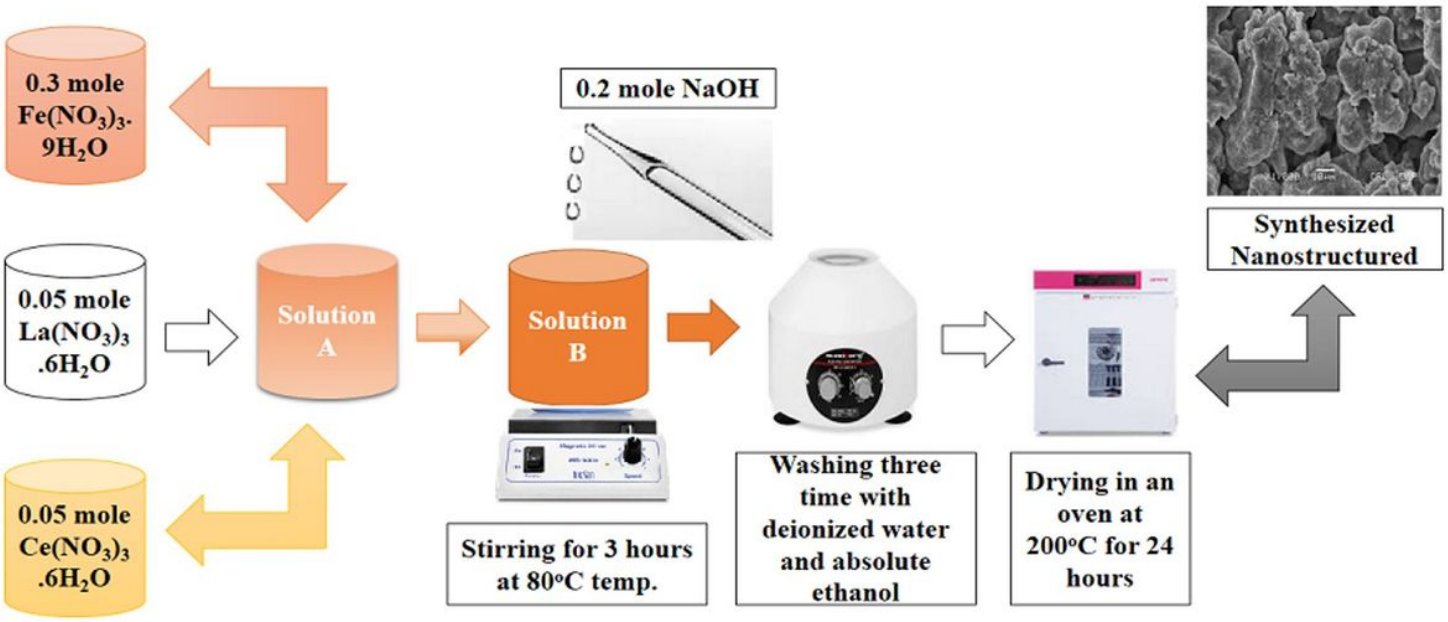

Figure 1

Schematic diagram of co-precipitate method

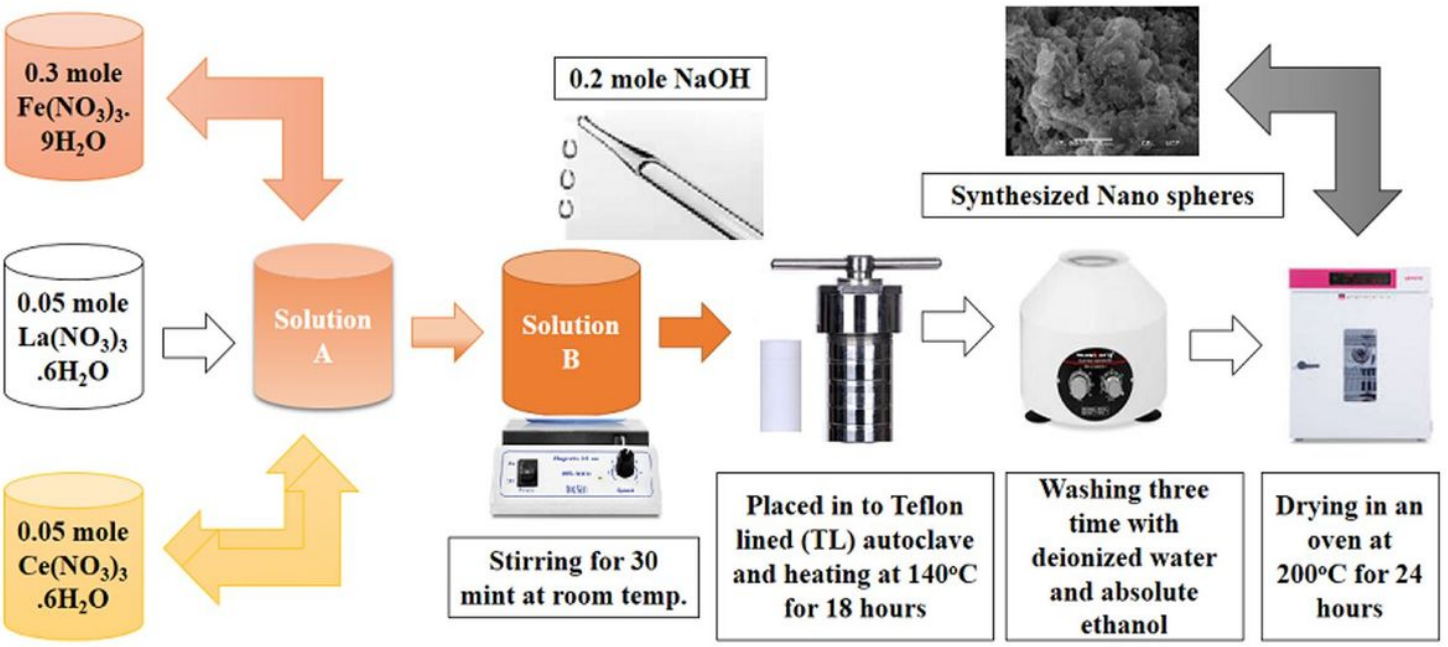

Figure 2

Schematic diagram of hydrothermal method

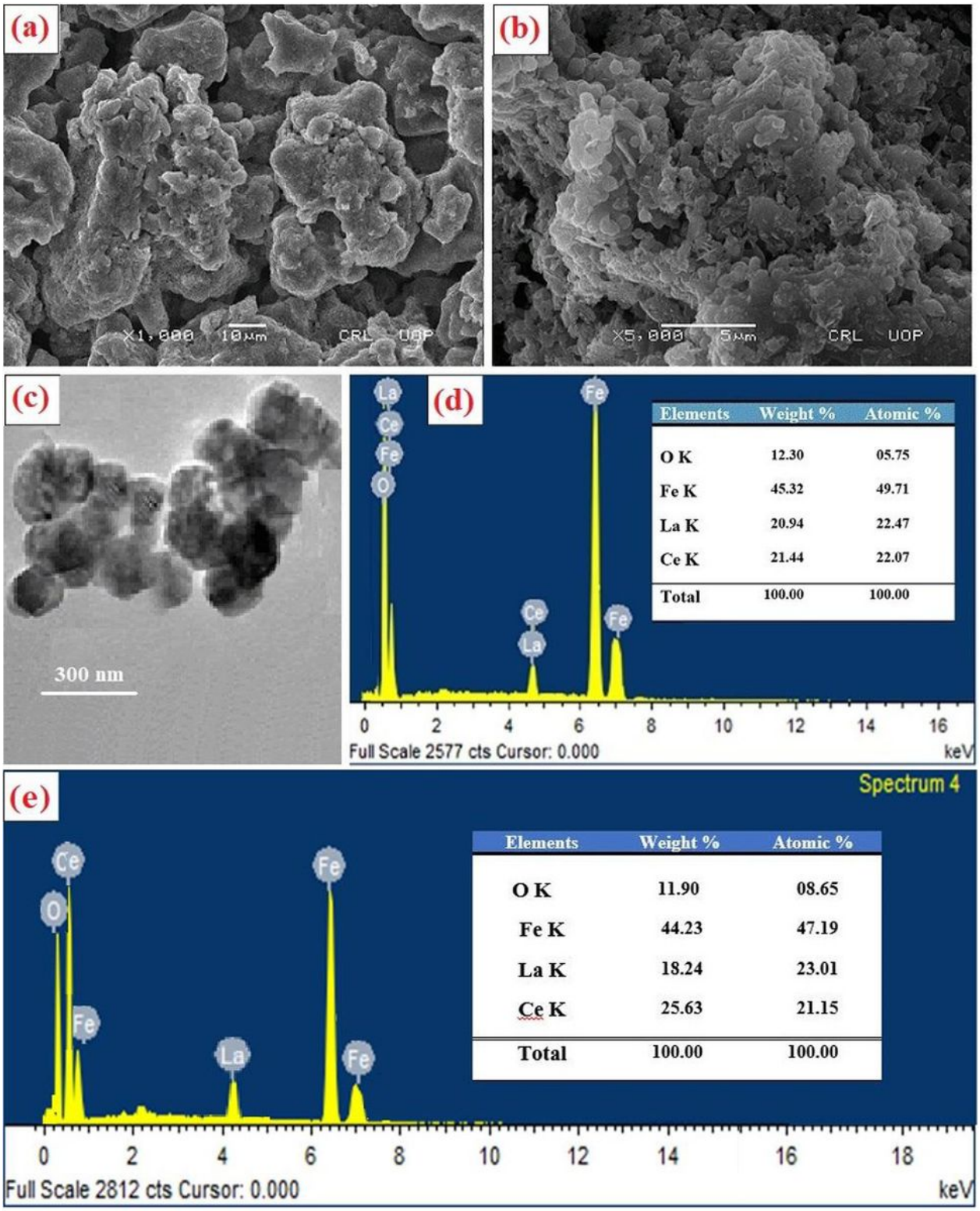

Figure 3

(a-b) SEM micrographs of J1 and J2 nanostructures, (c) TEM image of J2 nanostructures and (d-e) EDX spectrum of J1 and J2 nanostructures.

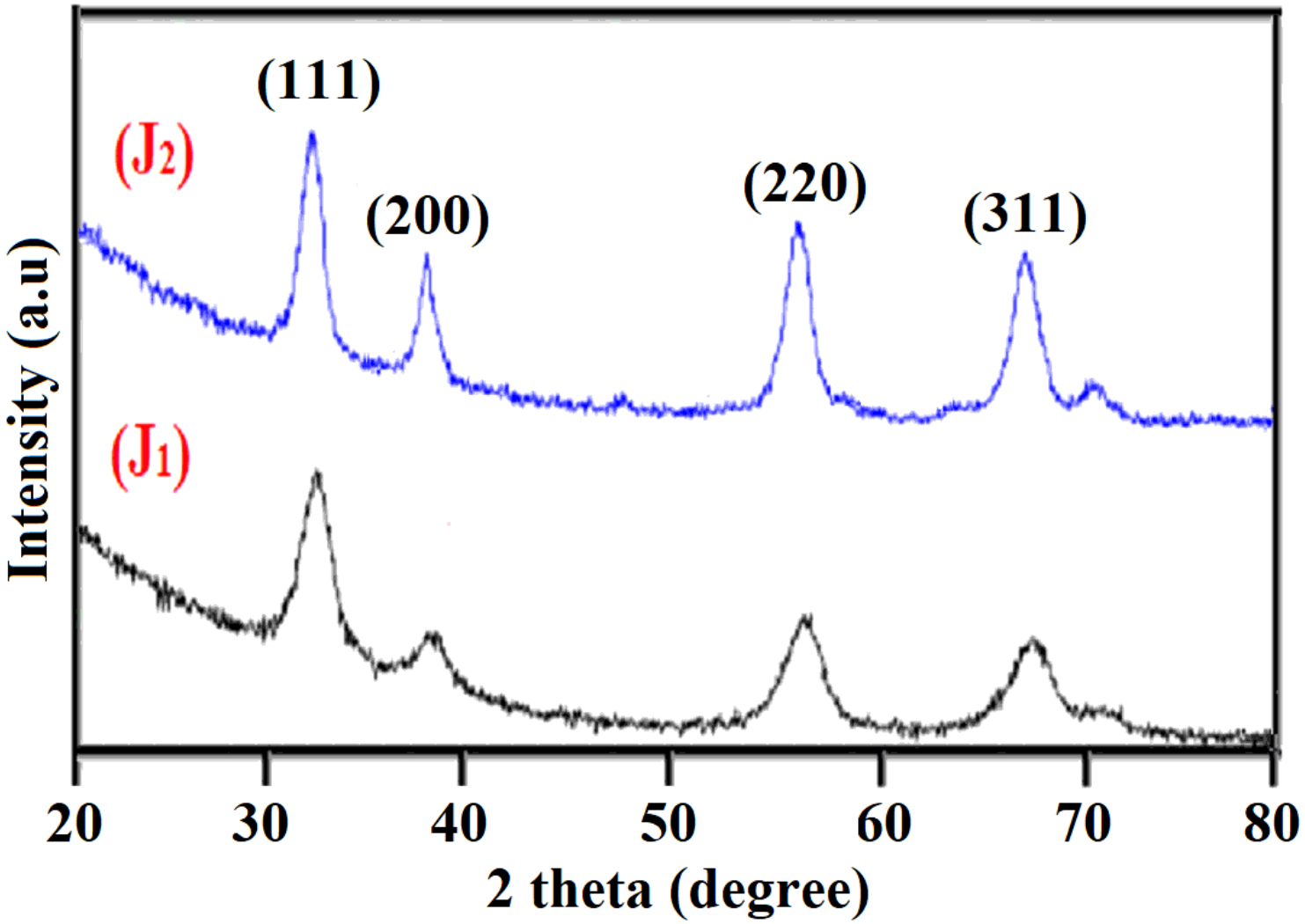

Figure 4

X-rays diffraction patterns of J1 and J2 nanoparticles.

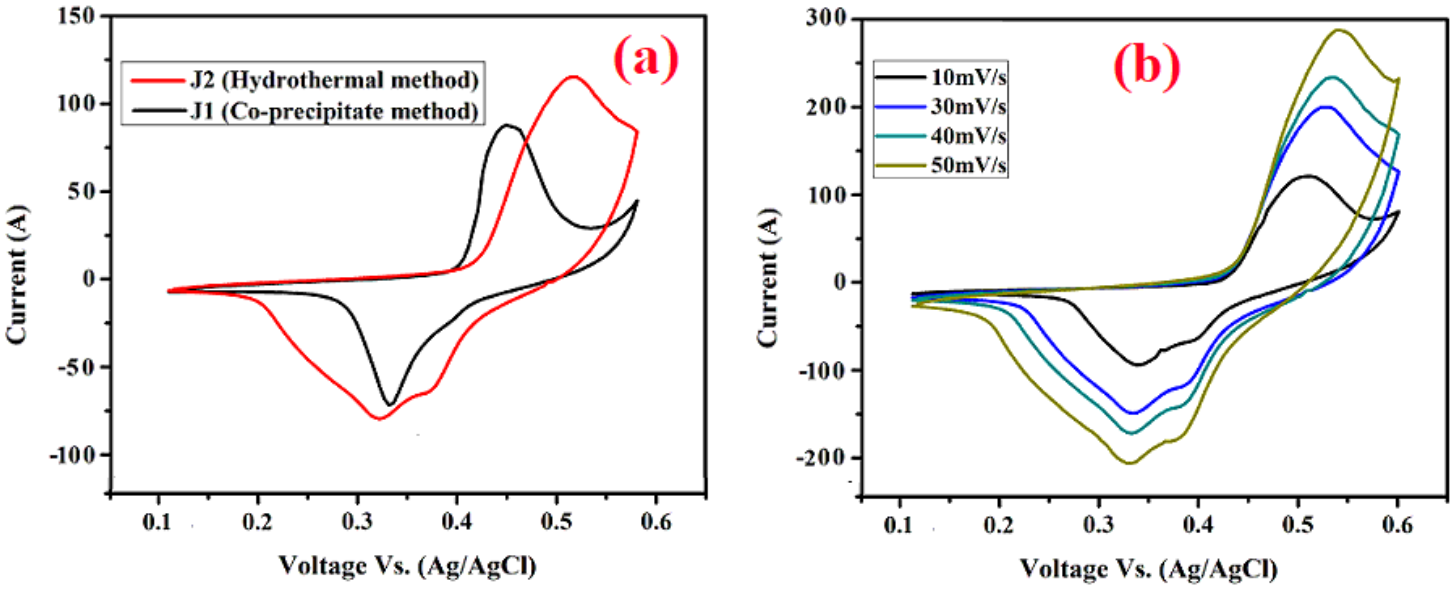

Figure 5

(a) Comparative CV curves of J1 and J2 electrodes at scan rate of 15mV/s in the potential range of 0.1-0.6 V in 6 M KOH electrolyte (b) CV curves of J2 electrode at different scan rates.

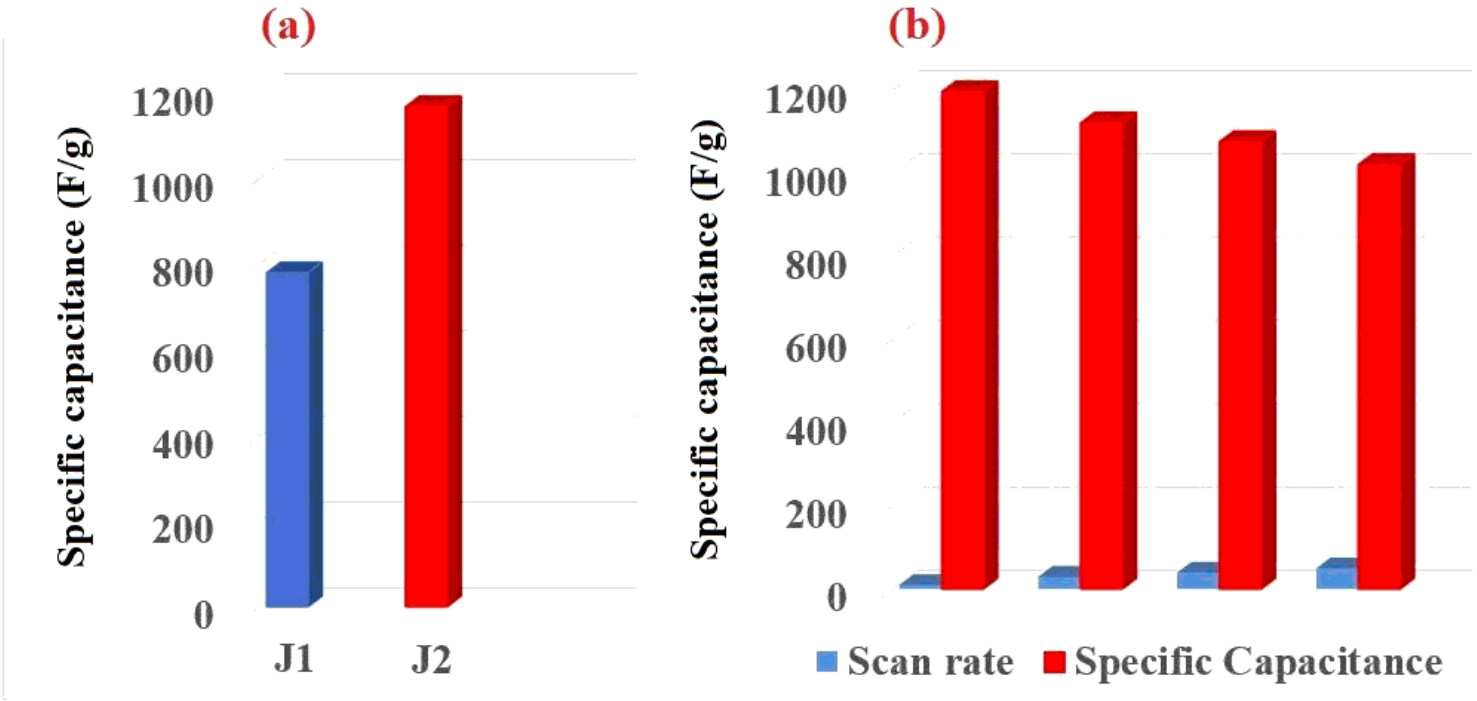

Figure 6

(a) Comparative specific capacitance Csp (F/g) of J1 and J2 electrodes at scan rate of 15mV/s in the potential range of 0.1-0.6 V in 6 M KOH electrolyte (b) Variation specific capacitance Csp (F/g) vs. different scan rates for J2 sample.

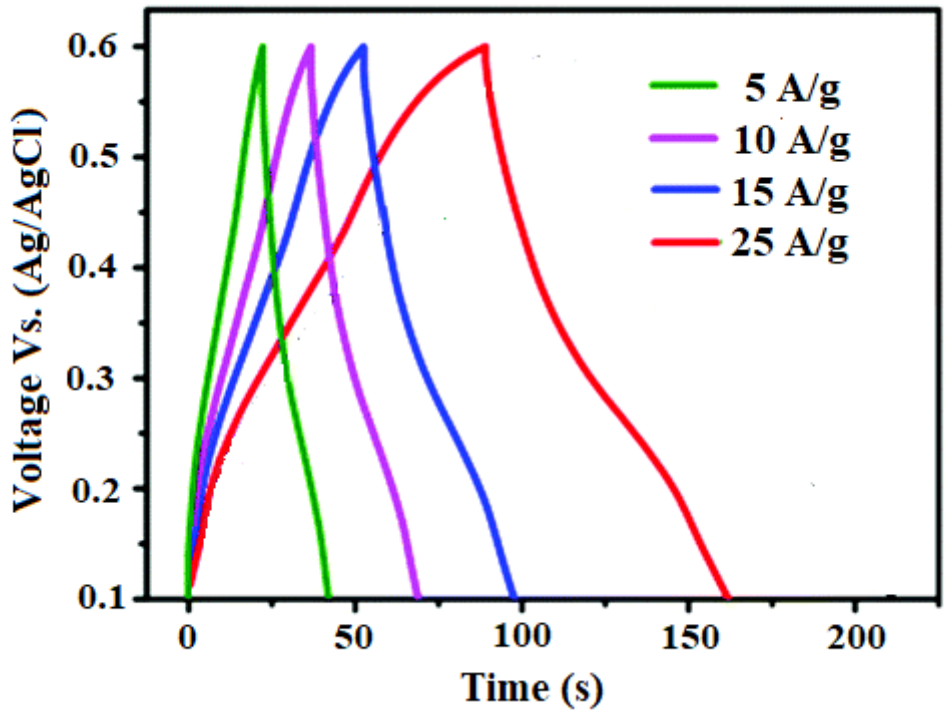

Figure 7

GCD curves of J2 electrode at different current densities in the potential range of 0.1-0.6 V in 6 M KOH electrolyte.

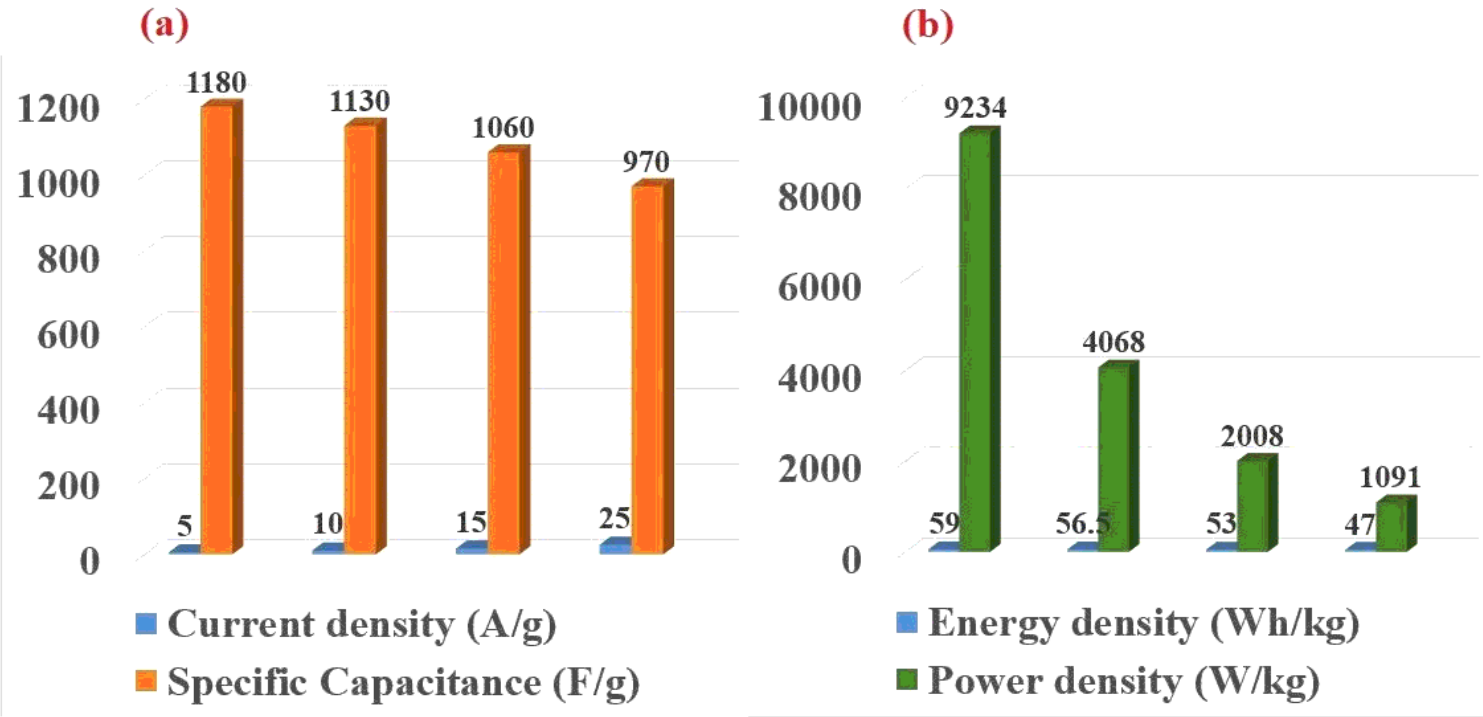

Figure 8

(a) Variation specific capacitance Csp (F/g) vs. different current densities for J2 electrode (b) Ragone plot for J2 sample.

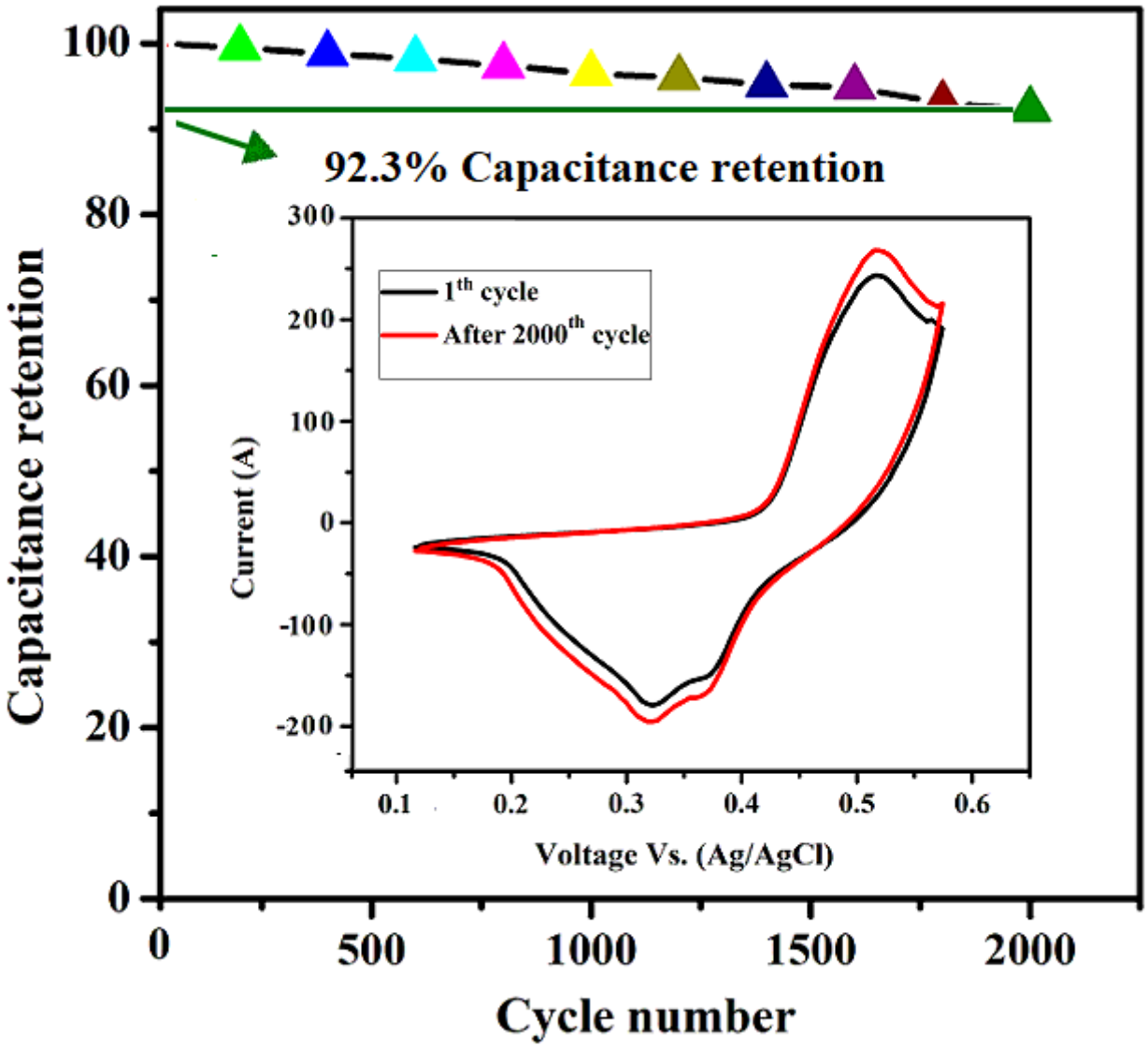

Figure 9

The cycling performance of J2 electrode at a scan rate of 20 mV/s in 6 M KOH electrolyte

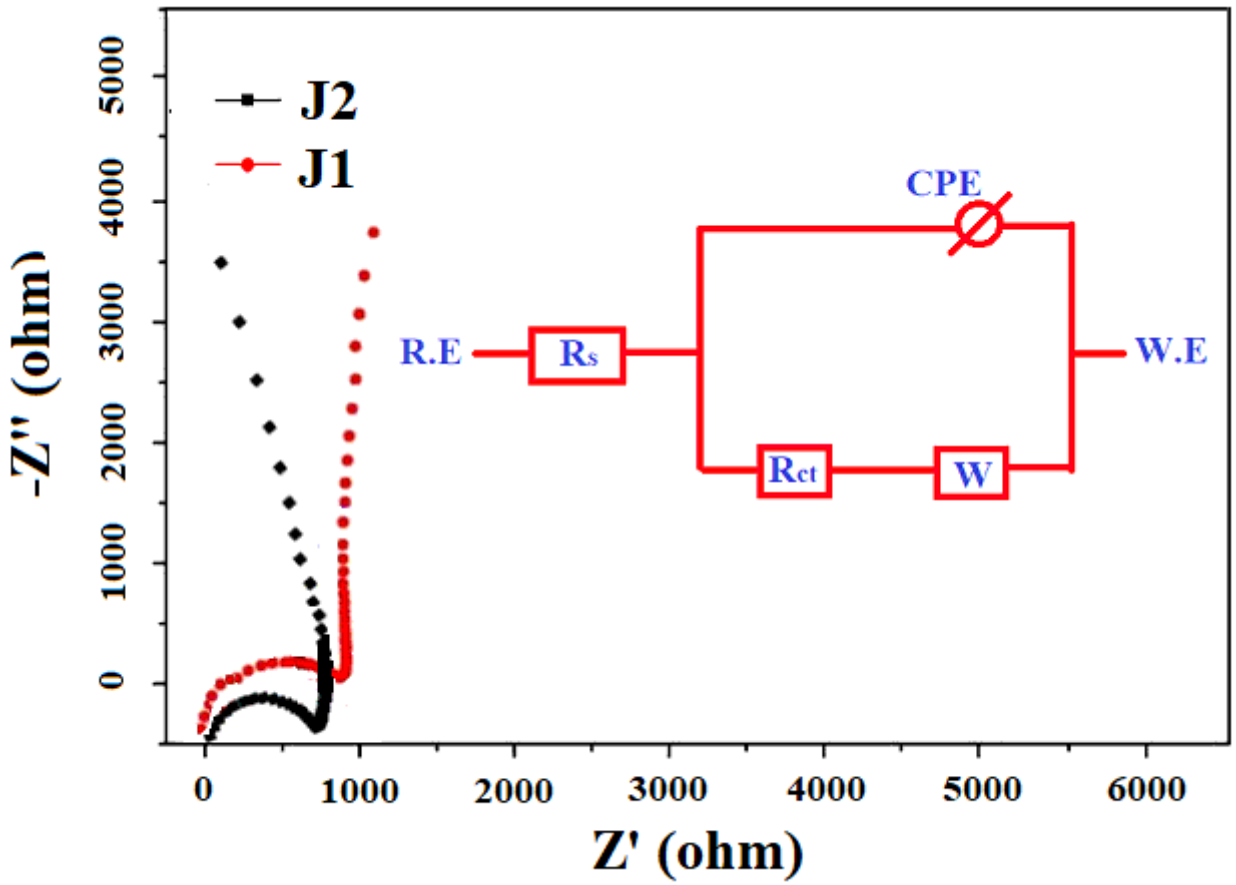

Figure 10

Nyquist plot and the inset fitted equivalent circuit